



HAL
open science

**Regolith evolution on the millennial timescale from
combined U-Th-Ra isotopes and in situ cosmogenic ¹⁰
Be analysis in a weathering profile (Strengbach
catchment, France)**

Julien Ackerer, François Chabaux, Jerome van Der Woerd, Daniel Viville, Eric
Pelt, Elise Kali, Catherine Lerouge, Philippe Ackerer, Raphael Di Chiara
Roupert, Philippe Négrel

► **To cite this version:**

Julien Ackerer, François Chabaux, Jerome van Der Woerd, Daniel Viville, Eric Pelt, et al.. Regolith evolution on the millennial timescale from combined U-Th-Ra isotopes and in situ cosmogenic ¹⁰ Be analysis in a weathering profile (Strengbach catchment, France). *Earth and Planetary Science Letters*, 2016, 453, pp.33-43. 10.1016/j.epsl.2016.08.005 . hal-03885476

HAL Id: hal-03885476

<https://hal.science/hal-03885476>

Submitted on 5 Dec 2022

HAL is a multi-disciplinary open access archive for the deposit and dissemination of scientific research documents, whether they are published or not. The documents may come from teaching and research institutions in France or abroad, or from public or private research centers.

L'archive ouverte pluridisciplinaire **HAL**, est destinée au dépôt et à la diffusion de documents scientifiques de niveau recherche, publiés ou non, émanant des établissements d'enseignement et de recherche français ou étrangers, des laboratoires publics ou privés.

1 **Regolith evolution on the millennial timescale from combined U-Th-Ra isotopes and in situ**
2 **cosmogenic ¹⁰Be analysis in a weathering profile (Strengbach catchment, France)**

3

4

5 J. Ackerer *(1), F. Chabaux *(1), J. Van der Woerd (2), D. Viville (1), E. Pelt (1), E. Kali (2), C.
6 Lerouge (3), P. Ackerer (1), R. di Chiara Roupert (1), P. Négrel (3).

7

8

9 (1) Laboratoire d'Hydrologie et de Géochimie de Strasbourg, CNRS UMR 7517, University
10 of Strasbourg (LHyGeS, 1 rue Blessig, 67084 Strasbourg cedex, France).

11 (2) Institut de Physique du Globe de Strasbourg, CNRS UMR 7516, University of
12 Strasbourg (IPGS, 5 rue René Descartes, 67084 Strasbourg cedex, France).

13 (3) BRGM, 3 Avenue Claude Guillemin, 45060 Orléans, France.

14

15 **Abstract : 352 words**

16 **Text (without acknowledgment): 6538 words**

17

18

19

20 **Corresponding Authors: fchabaux@unistra.fr, julien.ackerer2@etu.unistra.fr**

21

22 **Abstract**

23 U-Th-Ra disequilibria, cosmogenic in situ ^{10}Be concentrations and major and trace element
24 concentrations have been analyzed in a 2 m-deep weathering profile sampled at the summit
25 of the granitic Strengbach catchment (France). The data have been used to independently
26 estimate both the long-term regolith production and denudation rates and the weathering
27 and erosion rates. Modeling of the ^{238}U - ^{234}U - ^{230}Th - ^{226}Ra disequilibrium variations in the
28 lower part of the profile yields a regolith production rate of 12 ± 4 mm/kyr (30 ± 10 T/km²/yr),
29 while modeling of the high-resolution ^{10}Be concentration profile leads to an exposure age of
30 19.7 ± 2.2 kyr, an inherited concentration of $15,000\pm 1,000$ at/g in quartz and a mean
31 denudation rate of 22 ± 10 mm/kyr (37 ± 15 T/km²/yr). The consistency between production
32 and denudation rates suggests that, on a millennial timescale, the regolith mass balance at
33 the summit of the catchment is close to a steady state, even if the watershed may have been
34 impacted by Quaternary climatic changes and by recent anthropogenic perturbations (e.g.,
35 20th century acid rain and recent afforestation efforts). The results also indicate that physical
36 erosion is likely the dominant long-term process of regolith denudation in the catchment.
37 Furthermore, the comparison of the long-term production and denudation rates and of
38 weathering and erosion rates determined from the depth profile analyses with the current
39 weathering and erosion rates estimated at the outlet of the watershed based on monitoring
40 of the water chemistry and sediment fluxes suggests that physical erosion may have varied
41 more than the chemical weathering flux during the last 150 kyr. Although very few other
42 sites with U-series, in situ ^{10}Be and stream monitoring data are available for comparison, the
43 current data suggest that (1) the mass balance steady state of regolith might be commonly
44 achieved in soil mantled landscapes and (2) physical erosion has varied much more than
45 chemical weathering in mid-mountain catchments over the last 10-150 kyr. These results
46 highlight the importance of the combined analysis of U-series nuclides and in situ ^{10}Be in the
47 same weathering profile for the determination of key geomorphic parameters, which are
48 important to constraining landscape stability and the responses of landscapes to natural or
49 anthropogenic forcing.

50 **Keywords**

51 Regolith, weathering, denudation, U-series nuclides, in situ ^{10}Be .

52 **1- Introduction**

53 Regolith production and denudation rates, which correspond to the rate at which bedrock is
54 weathered into mobile regolith and removed by chemical and physical processes, are key
55 parameters in the evaluation of landscape stability and the responses of landscapes to
56 natural or anthropogenic forcing (e.g., Brantley et al., 2007; Banwart et al., 2011). The
57 analytical developments made over the last decades for precisely analyzing the U-series
58 nuclides (i.e., ^{238}U - ^{234}U - ^{230}Th) in geological and environmental samples have led to the
59 development of the study of U-series nuclides in soils and weathering profiles and to the
60 definition of a theoretical framework for quantifying regolith production rates from the
61 variations in radioactive disequilibria along a weathering profile (Dequincey et al., 2002;
62 Chabaux et al., 2003, 2013; Dosseto et al., 2008, 2012; Ma et al., 2010). These studies were
63 mainly based on the analysis of ^{238}U - ^{234}U - ^{230}Th nuclides and the use of the activity ratios
64 ($^{234}\text{U}/^{238}\text{U}$)-($^{230}\text{Th}/^{234}\text{U}$) (activity ratios will be noted hereafter with parentheses). More
65 recently, some studies have also included the analysis of the ^{226}Ra nuclide and hence the use
66 of the ($^{226}\text{Ra}/^{230}\text{Th}$) ratio (Chabaux et al., 2013; Gontier et al., 2015). Similarly, the in situ ^{10}Be
67 depth profile methodology has enabled the estimation of both exposure age and mean
68 denudation rate from cosmogenic isotope inventories (e.g., Brown et al., 1995; Braucher et
69 al., 2009). This approach has been widely used to constrain the ages of alluvial terraces and
70 fans (Anderson et al., 1996; Schaller et al., 2002; Brocard et al., 2003), as well as the long-
71 term denudation rates of regolith (Small et al., 1999; Heimsath et al., 2000; Ferrier and
72 Kirchner, 2008; Cui et al., 2016). However, very few studies have combined a detailed
73 analysis of U-Th-Ra isotopes with cosmogenic in situ ^{10}Be in a single weathering profile
74 extending from the topsoil to the bedrock. It is the aim of this work to highlight the potential
75 of combining these two approaches to independently constrain both production and

76 denudation rates of regolith and to show that information associated with geochemical
77 mobility can be used to discuss the long-term evolution of the regolith.

78 **2- Site presentation and sampling strategy**

79 The study is performed on the Strengbach catchment, which constitutes the “Observatoire
80 Hydrogéochimique de l’Environnement” (OHGE), one of the French critical zone
81 observatories (<http://rnbv.ipgp.fr>). It is a small watershed of 0.8 km² located in the Vosges
82 massif (northeastern France; Figure 1A). With altitudes ranging from 883 to 1147 m (Figures
83 1B and 1C), the current climate is mountainous-oceanic, with a mean annual rainfall and
84 temperature of 1400 mm and 6°C, respectively (Viville et al., 2012). The Vosges massif
85 experienced Pleistocene glaciations in a similar way to other central European mountains,
86 such as the Black Forest and the Bavarian Forest (Heyman et al., 2013). In accordance with
87 regional climatic studies (e.g., Leroy et al., 2000), cold conditions probably persisted at the
88 altitude of the Strengbach catchment well after the Late Glacial Maximum (LGM), and the
89 Vosges forest cover likely developed only at the onset of the Holocene. The Strengbach site
90 has been affected by anthropogenic deforestation associated with pastoralism, likely
91 beginning in the Bronze Age and lasting until the end of the 19th century (Etienne et al.,
92 2013). In the 20th century, the lower grazing pressure led to natural and artificial
93 afforestation in several places in the Vosges massif. In the Strengbach catchment, the return
94 to a densely forested cover is due to the planting of spruce stands at the beginning of the
95 20th century. The catchment is currently covered with a mixed spruce and beech forest
96 interspersed with small clearings. The bedrock is a base-poor late Hercynian granite and is
97 covered by a 50 to 100 cm-thick brown acidic soil (Hyperdystric Cambisol ; WRB 2006). The
98 granitic bedrock was hydrothermally overprinted, with the degree of hydrothermal

99 alteration decreasing from the northern to the southern part of the watershed (Fichter et al.,
100 1998).

101 To investigate the recent Quaternary weathering of the granitic bedrock and the denudation
102 rate of the soil, a sampling profile has been collected on the summit of the less
103 hydrothermally altered part of the watershed. This location avoids the presence of colluvial
104 deposition and corresponds to the best strategy ensuring that saprolite and soil are
105 genetically linked to the underlying bedrock and likely formed along the main vertical
106 weathering direction. A 2 m-deep and 3 m-wide pit was dug, and the samples were collected
107 in the middle part of the pit front (Figure 1D). Thirty-two bulk samples of ≈ 5 kg each were
108 collected along the profile with a sample every 5 cm within the soil and the saprolite and
109 every 10 cm within the fractured bedrock. The large mass collected per sample is necessary
110 to ensure a representative analysis of the weathering profile developed on the coarse-
111 grained granite (Gy, 1992). For each sample in the upper part of the profile (0-100 cm), the
112 fine fraction density was obtained by weighing a known volume of soil sampled with a steel
113 cylinder. The proportion of blocks, defined here as coarse fragments (>10 cm), was
114 estimated via macroscopic description and photos. The bulk density of each sample was
115 then calculated by combining the fine fraction density and the density of blocks with respect
116 to the proportion of blocks in the horizon. For the blocks, a constant density of 2700 kg/m^3 is
117 used, on the basis of granitic bedrock density measurements. A sequential crushing and
118 rigorous quartering process was then performed to obtain representative subsamples for
119 mineralogical analyses by X-ray diffraction (XRD), and for geochemical and isotopic analyses.

120 **3- Analytical methods**

121 **3.1 Mineralogical and major and trace element analysis**

122 The determination of the sample mineralogical compositions are given in Electronic
123 Appendix A. Six thin sections of rock samples were collected at regular intervals within the
124 granitic bedrock (Figure 1D). Major and trace element concentrations of the samples were
125 analyzed following the technique classically used at the LHyGeS (Strasbourg, France; e.g.,
126 Prunier et al., 2015). The quality of the analysis was checked by measuring the San Joaquin
127 soil standard (NIST SRM 2709a). The overall uncertainty is <5 % for the major element and
128 <10 % for the trace element concentrations (Table 1).

129 **3.2 U-Th-Ra isotopes**

130 For the U-Th-Ra analysis, each subsample consists of approximately 100 mg of 53 μm
131 powdered bulk sample. Subsamples were weighed and spiked with both a mixed artificial
132 ^{233}U - ^{229}Th spike and a ^{228}Ra enriched spike to measure the isotopic ratios and U-Th-Ra
133 concentrations by isotopic dilution, using the protocol developed in the LHyGeS (Strasbourg,
134 France; Granet et al., 2010; Chabaux et al., 2013; Pelt et al., 2013). The powders were first
135 digested in PFA beakers using combinations of HF, HNO_3 , HCl, HClO_4 and H_3BO_3 acids at 100-
136 200°C, and U, Th, and Ra were then separated and purified by ion exchange chromatography
137 using Biorad anionic resin. U and Th isotopes were measured on a plasma mass spectrometer
138 (MC-ICP-MS Neptune), and the ^{226}Ra isotope was measured on a thermal ionization mass
139 spectrometer (TIMS Triton, Table 2). The precision and accuracy of the analyses are checked
140 by regular analysis of liquid standards (HU1 U, IRMM036 Th and ^{228}Ra -spike), the rock
141 standard BCR-2 and sample replicates. The ($^{234}\text{U}/^{238}\text{U}$) activity ratio was 0.9992 ± 0.0018 for
142 HU1 (2σ , N=19) and the $^{232}\text{Th}/^{230}\text{Th}$ isotope ratio was 326284 ± 2855 for IRMM036 (2σ , N=21).
143 The ($^{234}\text{U}/^{238}\text{U}$), ($^{230}\text{Th}/^{234}\text{U}$), ($^{230}\text{Th}/^{232}\text{Th}$) and ($^{226}\text{Ra}/^{230}\text{Th}$) activity ratios for BCR-2 were
144 1.0028 ± 0.0018 , 1.0045 ± 0.0104 , 0.8824 ± 0.0076 and 0.9946 ± 0.0078 (2σ , N=2), respectively.

145 The mean U and Th blank concentrations were 46 pg and 157 pg, respectively, whereas the
146 Ra concentrations were below the detection limit. These blank concentrations were all
147 negligible compared to the measured quantities of U, Th and Ra. Inter-session standard and
148 duplicate measurements enabled estimation of the analytical uncertainty in the calculated U-
149 Th-Ra radioactive activity ratios. The analytical uncertainty is 0.2 % for ($^{234}\text{U}/^{238}\text{U}$), 1.5 % for
150 ($^{230}\text{Th}/^{234}\text{U}$) and 1.7 % for ($^{226}\text{Ra}/^{230}\text{Th}$) activity ratios.

151 **3.3 In situ ^{10}Be isotope**

152 For the in situ ^{10}Be analysis, each subsample consists of 150 g of 250-500 μm sieved powder
153 obtained from quartering the 2 mm crushed bulk samples. Oxides and organic matter were
154 removed by HCl leaching, and a sequential HF dissolution was performed to remove the
155 meteoric ^{10}Be and obtain purified quartz (e.g., Nishiizumi et al., 1989). After addition of a ^9Be
156 carrier, the purified quartz was dissolved, and beryllium separation and purification were
157 performed by ion exchange chromatography. After hydroxylation and targeting, the $^{10}\text{Be}/^9\text{Be}$
158 ratios were measured by accelerator mass spectrometry at ASTER (CEREGE, University of Aix-
159 Marseille, France). The $^{10}\text{Be}/^9\text{Be}$ ratios of the blanks and samples are approximately 1×10^{-15}
160 and 1×10^{-13} , respectively. The overall analytical uncertainty is <5 % for the calculated ^{10}Be
161 concentrations (Table 3).

162 **4- Determination of the regolith production rate, denudation rate and chemical mobility**

163 **4.1 Regolith production rate from U-Th-Ra disequilibria**

164 The principle of determination of the regolith production rate from the analysis of U-Th-Ra
165 disequilibria has been detailed in previous studies (e.g., Dosseto et al., 2008, 2012; Ma et al.,
166 2010; Chabaux et al., 2011, 2013). The approach is based on the analysis of samples
167 collected along the main weathering direction, in the present case the vertical direction. For

168 samples in the weathering zone, as the time variation of nuclide mobility during water rock
 169 interactions is not known *a priori*, the time evolution of radioactive nuclides, is classically
 170 described in terms of continuous processes involving, in addition to the radioactive decay
 171 laws, loss and gain processes represented by first-order kinetic rate laws for the loss
 172 processes and zero-order kinetic rate laws for the gain processes. For the ^{238}U - ^{234}U - ^{230}Th -
 173 ^{226}Ra system, this leads to the following equations:

$$\frac{d\ ^{238}\text{U}}{dt} = f_{238}\ ^{238}\text{U}_0 - k_{238}\ ^{238}\text{U} - \lambda_{238}\ ^{238}\text{U} \quad (1)$$

$$\frac{d\ ^{234}\text{U}}{dt} = f_{234}\ ^{234}\text{U}_0 + \lambda_{238}\ ^{238}\text{U} - k_{234}\ ^{234}\text{U} - \lambda_{234}\ ^{234}\text{U} \quad (2)$$

$$\frac{d\ ^{230}\text{Th}}{dt} = f_{230}\ ^{230}\text{Th}_0 + \lambda_{234}\ ^{234}\text{U} - k_{230}\ ^{230}\text{Th} - \lambda_{230}\ ^{230}\text{Th} \quad (3)$$

$$\frac{d\ ^{226}\text{Ra}}{dt} = f_{226}\ ^{226}\text{Ra}_0 + \lambda_{230}\ ^{230}\text{Th} - k_{226}\ ^{226}\text{Ra} - \lambda_{226}\ ^{226}\text{Ra} \quad (4)$$

174 where λ_i , k_i and f_i are the radioactive decay, loss and gain constants (in yr^{-1}), respectively, for
 175 the radionuclides i (i.e., ^{238}U , ^{234}U , ^{230}Th and ^{226}Ra). In the equations, t is the time elapsed
 176 between the reference weathering state and its current state. For simplification during the
 177 equation-solving procedure, the input fluxes are expressed as a proportion of the number of
 178 atoms of nuclides added per year to the initial sample. The loss (k) and gain (f) terms used in
 179 the equations are usually assumed to be constant with time for the purpose of simplicity and
 180 tractability (e.g., Dequincey et al., 2002; Dosseto et al., 2008; Ma et al., 2010; Chabaux et al.,
 181 2013). The mean production rate of regolith, P (in mm/kyr), can be estimated through the
 182 resolution of the above equation system and the determination of the age Δt (in kyr) of a
 183 sample relative to a reference sample from deeper in the profile at a distance Δh (in mm)

184 along the weathering direction. For isovolumetric weathering, P is given by the following
185 equation:

$$P = \frac{\Delta h}{\Delta t} \quad (5)$$

186

187 As the gain and loss coefficients in equations 1-4 are not known and the ^{238}U - ^{234}U - ^{230}Th - ^{226}Ra
188 analyses yield only three independent data per sample, namely the ($^{234}\text{U}/^{238}\text{U}$), ($^{230}\text{Th}/^{234}\text{U}$)
189 and ($^{226}\text{Ra}/^{230}\text{Th}$) ratios, the analysis of only one sample (in addition to a reference sample) is
190 not sufficient to determine the weathering production rate P. The mathematical formalism
191 developed to retrieve such time information assumes that the gain and loss coefficients (k_i
192 and f_i) of the model can be considered constants, at least for a part of the profile from which
193 several different samples can be collected and analyzed. The measured ($^{234}\text{U}/^{238}\text{U}$),
194 ($^{230}\text{Th}/^{234}\text{U}$) and ($^{226}\text{Ra}/^{230}\text{Th}$) ratios of each sample are used to determine the mobility
195 parameters of the model and the age of different samples relative to the reference sample.
196 The numerical solutions are obtained using a stochastic quantum particle swarm
197 optimization scheme (more details in Chabaux et al., 2013), which minimizes the sum of the
198 squared differences between the measured and estimated activity ratios. The parameter
199 solutions that allow the model to fit the observed activity ratios within 1 % error are
200 retained and averaged to obtain a set of optimized output parameter values. The
201 uncertainties in the parameter estimates are calculated as two-sigma standard deviations on
202 the mean parameter estimate. It is important to stress here that such modeling approaches
203 only give mean long-term values, i.e., over several kyr or 10 kyr, for regolith production rates
204 and nuclide gain and loss parameters.

205 **4.2 Regolith denudation rate from in situ ^{10}Be depth profile**

206 As with U-series disequilibrium methodology for regolith production rate, the depth
 207 variations of in situ ¹⁰Be concentrations within a weathering profile are recognized as a
 208 powerful approach to constrain geomorphologic parameters, including the mean
 209 denudation rate of a regolith (e.g., Siame et al., 2004; Dosseto and Schaller, 2016). In situ
 210 ¹⁰Be is produced at the surface of the Earth by the interaction of cosmic rays and rock atomic
 211 nuclei (Brown et al., 1995). By taking into account (1) the different attenuation lengths of
 212 secondary neutrons and muons, which produce ¹⁰Be mainly in surface horizons for neutrons
 213 and at greater depths for muons (Kim and Englert, 2004), and (2) their relative contribution
 214 to the total produced ¹⁰Be, the depth variations of in situ ¹⁰Be concentrations within a
 215 weathering profile is given by (e.g., Siame et al., 2004; Braucher et al., 2009):

$$\begin{aligned}
 C(t, d, z) = & C_0 \exp(-\lambda t) + \frac{P_0 * P_n}{\frac{\rho d}{K_n} + \lambda} \exp\left(\frac{-\rho z}{K_n}\right) \left(1 - \exp\left(-t\left(\frac{\rho d}{K_n} + \lambda\right)\right)\right) \\
 & + \frac{P_0 * P_{nm}}{\frac{\rho d}{K_{nm}} + \lambda} \exp\left(\frac{-\rho z}{K_{nm}}\right) \left(1 - \exp\left(-t\left(\frac{\rho d}{K_{nm}} + \lambda\right)\right)\right) \\
 & + \frac{P_0 * P_{fm}}{\frac{\rho d}{K_{fm}} + \lambda} \exp\left(\frac{-\rho z}{K_{fm}}\right) \left(1 - \exp\left(-t\left(\frac{\rho d}{K_{fm}} + \lambda\right)\right)\right) \quad (6)
 \end{aligned}$$

216 where t is the exposure age of the profile (in yr), d is the mean denudation rate (in cm/yr), z
 217 is the depth of each sample (in cm), C_0 is the initial concentration from previous exposure (in
 218 atoms/g quartz), λ is the radioactive decay of the ¹⁰Be (in yr⁻¹) and ρ is the integrated density
 219 of each sample (in g/cm³). P_0 is the total production rate of ¹⁰Be at the surface of the soil
 220 (12.17 at/g/yr and 0.266 at/g/yr for spallation and muons, respectively, determined with the
 221 CRONUS online calculator; Balco et al., 2008). P_n , P_{nm} and P_{fm} are the relative contributions
 222 of 97.85, 1.5 and 0.65 % to the total production and K_n , K_{nm} and K_{fm} are the effective

223 attenuation lengths of 150, 1500 and 5300 g/cm², for secondary neutrons, negative muons
224 and fast muons, respectively (Braucher et al., 2009). The depth variations of in situ ¹⁰Be
225 concentrations in a weathering profile can thus be used to estimate the exposure age and
226 the mean denudation rate of a regolith, in addition to the inherited ¹⁰Be concentration,
227 without any steady state assumption.

228 **4.3 Chemical mobility and volumetric variation**

229 In addition to the determination of regolith production and denudation rates from the above
230 approaches, the chemical mobility and volumetric variation associated with the weathering
231 processes can be estimated through the analysis of major and trace element concentrations.
232 Based on the presence of an immobile element *j*, the chemical mobility of an element *i*
233 during weathering can be quantified by mass transfer coefficients (Brimhall et al., 1991), as
234 defined by the following:

$$\tau_i = \left(\frac{C(i)_{sample} * C(j)_{bedrock}}{C(i)_{bedrock} * C(j)_{sample}} - 1 \right) \quad (7)$$

235
236 where $C(i)_{sample}$ and $C(i)_{bedrock}$ represent the concentrations of the element *i* for a given
237 sample and for the deepest bedrock sample and $C(j)_{sample}$ and $C(j)_{bedrock}$ represent the
238 concentrations of the immobile element *j* for a given sample and for the deepest bedrock
239 sample, respectively. Positive or negative τ_i values imply the gain or loss, respectively, of the
240 element *i* relative to the deepest bedrock sample, taken here as the reference rock. In
241 addition, the chemical depletion fraction (Riebe et al., 2003), allows an estimation of the
242 denudation fraction due to chemical weathering between the reference bedrock sample and
243 a given sample and is defined by the following:

$$CDF = \left(1 - \frac{C(j)_{bedrock}}{C(j)_{sample}} \right) \quad (8)$$

244 It is also possible to estimate the relative volume variation associated with rock weathering
245 between two considered levels by the volumetric strain index calculation (Brimhall et al.,
246 1991; Riebe et al., 2003):

247

$$\varepsilon = \left(\frac{C(j)_{bedrock} * d_{bedrock}}{C(j)_{sample} * d_{sample}} \right) - 1 \quad (9)$$

248

249 where $d_{bedrock}$ and d_{sample} are the bulk density values of the bedrock and the considered
250 sample, respectively. Values of ε close to zero imply isovolumetric weathering, while positive
251 or negative values indicate expansion or compaction, respectively.

252 **5- Results**

253 **5.1 Mineralogical and geochemical variations within the weathering profile**

254 The whole rock XRD analyses are presented in Appendix A and in Table EA1. These data
255 along with the thin section observations are consistent with previously published data for
256 the Strengbach site (e.g., Fichter et al., 1998) and indicate that quartz and muscovite do not
257 present any significant evidence of weathering in the granitic bedrock. Biotite is weathered
258 at all depths and replaced by clays, sericite and hematite. The K-feldspar and plagioclase
259 crystals show structural and mineralogical evolution from the base to the top of the granite,
260 with a higher density of clay filled cracks in samples from the granite top. Carlsbad and
261 polysynthetic twins are identifiable at the granite base, while it is more difficult to recognize
262 them at the granite top. The analysis of the <2 μm clay fraction (Table EA1) indicates that the

263 clay composition is relatively homogeneous within the granitic bedrock and is dominated by
264 illite (40 to 60 % illite, 20 to 30 % inter-stratified illite/smectite, 5 to 25 % of smectite and 5
265 to 10 % of kaolinite). The clay composition is different and more variable in the soil, where
266 the smectite and inter-stratified clays become dominant (60 to 70 %) followed by the illite
267 (20 to 30 %) and kaolinite (5 to 10 %). These data show a significant increase in supergene
268 alteration from the base to the top of the profile, in accordance with the increase in the loss
269 on ignition (LOI, Table 1).

270 The variations in the major and trace element concentrations within the weathering profile
271 (Table 1) have been used to estimate the chemical mobility associated with weathering by
272 the calculation of the mass transfer coefficients. For this calculation, Ti is often considered
273 one of the best-suited immobile elements (e.g., Egli et al., 2006). For the tau calculation, the
274 normalization to Ti rather than to Zr concentration has been preferred, even if Zr can be
275 considered immobile in such environment (Rihs et al., 2011). The reason is the better
276 analytical precision obtained for the Ti concentrations (3%) than for Zr ($\approx 10\%$), which leads
277 to a better precision of the tau value determined with Ti ($\approx 10\%$) than with Zr ($\approx 20\%$). The
278 calculation of relatively constant ratios within the profile between Ti and other elements
279 usually considered immobile, such as Ta (not shown) and Th (Figure 2c), especially in the
280 deeper part of the profile, reinforces the assumption that Ti is mainly immobile during
281 weathering. Tau values indicate no significant mobility for the main major elements (Na_2O ,
282 K_2O , CaO , Al_2O_3 , and SiO_2) in the deeper part of the granitic profile below 100 cm depth
283 (Figure 2a). The depletion becomes significant in the regolith portion above 100 cm depth,
284 with chemical mobility trends that differ from one element to another, especially in the
285 uppermost part of the soil known to be significantly affected by biological processes,
286 vegetation cycling and atmospheric deposition (e.g., Stille et al., 2011; Gangloff et al., 2014).

287 In this upper part of the profile, the volumetric strain index indicates a significant expansion
288 of the soil horizons, with ε values from 50 to 150 %, while deeper in the profile, in the
289 granite and saprolite horizons, the weathering is nearly isovolumetric (Figure 3b).

290 As for tau values, the depth variations in the U/Th concentration ratios measured by isotopic
291 dilution, which are more precisely estimated than the tau values, allow for subdividing the
292 profile into two main zones, with U loss in the lower part of the profile, which gradually
293 increases upwards up to approximately a depth of 100 cm, and a U/Th ratio increase toward
294 the surface above 100 cm (Figure 2b). This increase might indicate Th migration due to
295 complexation with organic colloids, as observed at other sites (Rihs et al., 2011), or U inputs
296 from external atmospheric deposition, as suggested in other contexts (Pelt et al., 2013;
297 Chabaux et al., 2013). Regardless of the precise origin of this increase, the U/Th data confirm
298 that the transition between granitic bedrock and regolith at a depth of approximately 100
299 cm vertically divides the weathering profile into two distinct zones that are marked by
300 different chemical mobility values and likely exhibit specific weathering processes.

301 **5.2 U-Th-Ra and in situ ¹⁰Be systematics**

302 The depth subdivision of the profile inferred from major and trace element mobility is also
303 observed in the U-Th-Ra disequilibrium data (Table 2, Figure 4). The lower part of the profile
304 (below 100 cm depth) is characterized by rather simple and continuous variation trends in
305 the (²³⁴U/²³⁸U), (²³⁰Th/²³⁴U) and (²²⁶Ra/²³⁰Th) activity ratios with depth, with an increase in
306 the (²³⁴U/²³⁸U) and (²³⁰Th/²³⁴U) ratios with decreasing depth and a decrease in the
307 (²²⁶Ra/²³⁰Th) ratios with decreasing depth (Figure 4). In the upper regolith, the (²³⁴U/²³⁸U)
308 and (²³⁰Th/²³⁴U) activity ratios define clearly opposite trends with depth, which support the
309 suggestion that the two parts of the profile are marked by different weathering processes.

310 The upper part of the profile is also characterized by much more scattered ($^{226}\text{Ra}/^{230}\text{Th}$)
311 ratios, without a simple correlation with depth.

312 For in situ ^{10}Be , the concentrations point to a progressive decrease with depth but with two
313 different patterns of variation in the profile, one in the deeper horizons, where the
314 weathering is isovolumetric, and the second one in the uppermost regolith horizons (<50
315 cm), which are affected by volumetric expansion (Table 3, Figure 3). The deeper part is
316 characterized by a common exponential decrease in ^{10}Be , while the soil to upper regolith
317 part (0-50 cm) is characterized by a linear decrease in the in situ ^{10}Be concentration with
318 depth (Figure 3).

319 **6. Discussion**

320 **6.1 Determination of regolith production and denudation rates**

321 The mineralogical and geochemical data lead to a depth-dependent division of the profile
322 into two main parts, with progressive variation trends of the U-series systematic in the
323 bedrock and more scattered variations in the upper horizons (Fig. 4). Similar to the results of
324 the analyses of the short half-life ^{228}Ra and ^{228}Th nuclides in soil profiles from different forest
325 catchments, including the Strengbach (Rihs et al., 2011; Gontier et al., 2015), the short-
326 distance variations in the upper horizons most likely result from preferential Th mobility
327 related to the differential mobilization of radionuclides in the presence of organic matter. As
328 also emphasized in Gontier et al., (2015), such short-distance redistributions in the soil
329 horizons may imply significant variability of the mobility coefficients in this part of the
330 profile, at least for Th isotopes. Thus, this effect prevents the direct application of the
331 radioactive disequilibrium methodology described in section 4-1. In the Strengbach case, and
332 likely in many other forest contexts, the bedrock is thus the most suitable place to quantify

333 the mean long-term regolith production rate via the conventional U-Th-Ra methodology. In
334 the present study, the modeling approach has been therefore applied only to the lower part
335 of the profile, in which Th can be assumed to be immobile (Figure 2c), consequently reducing
336 the number of unknowns in the modeling ($k_{230}=0$ and $f_{230}=0$). The modeling results (Figure 4)
337 show that the mean U mobility parameters fall within the range of existing data for shale
338 and granodiorite lithologies (Ma et al., 2010; Dequincey et al., 2002; Dosseto et al, 2008;
339 Chabaux et al, 2013). As evidenced by the obtained coefficients, the particular positive
340 correlation between $(^{234}\text{U}/^{238}\text{U})$ and $(^{230}\text{Th}/^{234}\text{U})$ ratios in the deeper part of the profile do
341 not correspond to a simple leaching of U. To explain the ratios of $(^{234}\text{U}/^{238}\text{U})>1$ and
342 $(^{230}\text{Th}/^{234}\text{U})>1$, U removal must have occurred at a higher rate than U input, and incoming U,
343 which may originate from U mobilization in the upper horizons, must have been
344 characterized by a higher ^{234}U - ^{238}U fractionation than the removed U (Figure 4, details also in
345 Dequincey et al., 2002). Such mobility implies precipitation of U-rich secondary minerals,
346 such as Fe-oxyhydroxides, from fluids with ratios of $(^{234}\text{U}/^{238}\text{U})>1$. This hypothesis is
347 supported by the ratios of $(^{234}\text{U}/^{238}\text{U})>1$ in soil solutions from a neighboring profile in the
348 same part of the watershed (Prunier et al., 2015). The U-Th-Ra modeling also gives the
349 elapsed time between the granite base and the lower regolith, which yields a mean regolith
350 production rate of 12 ± 4 mm/kyr. Considering the density of 2.5 for the lower regolith, the
351 regolith production rate in terms of specific flux is 30 ± 10 T/km²/yr.

352 For application of the in situ ¹⁰Be approach (section 4-2), a numerical inverse procedure has
353 been used to determine the exposure age, the mean denudation rate and the inherited
354 concentration that best explain the data from equation 6. The inverse procedure consists of
355 minimizing the chi-square value of the system by the algorithm of Levenberg-Marquardt

356 (Marquardt, 1963) and has been adapted to take into account the volumetric expansion of
357 the upper regolith. The chi-square value is defined as follows:

$$X = \sum \left(\frac{C_{data}(z) - (C_{model}(t, d, C_0, z) + \Delta C)}{\sigma(z)} \right)^2 \quad (10)$$

358

359 where $C_{data}(z)$ and $C_{model}(t, d, C_0, z)$ are the measured and modeled ^{10}Be concentrations,
360 respectively, and $\sigma(z)$ is the uncertainty in the measured ^{10}Be concentration for a sample at
361 depth z . A correction factor ΔC has been introduced to take into account the volumetric
362 expansion of the upper 50 cm because the density variation only is insufficient to explain the
363 concentration trend of this part of the profile. This implies that expansion must have
364 occurred relatively late (<5–10 kyr) in the history of the profile, as the measured
365 concentrations do not reflect the corresponding production rate changes. Uncertainty in the
366 parameters is estimated from the covariance matrix of the problem. It is important to stress
367 that, considering the mean denudation and the surface ^{10}Be production rates at the summit
368 of the Strengbach watershed, the current accumulation of ^{10}Be within the profile is not
369 balanced by erosion and radioactive decay. Because a ^{10}Be concentration steady state is not
370 present, the geochronometric application of the modeling is possible. The best fit gives an
371 exposure age of the profile of $19,734 \pm 2,168$ yr, a mean denudation rate of 22 ± 10 mm/kyr (in
372 terms of specific flux, 37 ± 15 T/km²/yr, based on the mean density of the regolith of 1.7) and
373 an inherited ^{10}Be concentration of $15,000 \pm 1,000$ at/g quartz (Figure 3).

374 **6.2 Implications for regolith evolution on the millennial timescale**

375 To the best of our knowledge, this study is likely the first one to combine U-series and in situ
376 ^{10}Be analyses on the same samples in a single weathering profile with such a depth extent

377 and spatial resolution. This coupled approach allows for determining, in addition to the
378 regolith denudation and production rates, the exposure age of the profile and the potential
379 ^{10}Be inherited concentration. As illustrated in the following, these estimates are relevant for
380 recovering the Quaternary dynamics of the weathering profile.

381 The determined exposure age inferred from the ^{10}Be data indicates the occurrence of an
382 erosive event at the summit of the Strengbach watershed approximately 20,000 yr ago, likely
383 resulting from glacial or peri-glacial processes in relation with the last Würm glaciation,
384 which is in accordance with regional investigations (Seret et al., 1990; Mercier et al., 1999).
385 In addition, the occurrence of an inherited ^{10}Be concentration within the bedrock indicates a
386 complex erosive history at the summit of the Strengbach catchment. By extrapolating the
387 long-term regolith propagation rate determined from U-Th-Ra variations (i.e., 30 ± 10
388 $\text{T}/\text{km}^2/\text{yr}$ or 12 ± 4 mm/kyr), an age of approximately 150 kyr is obtained for the entire 2 m-
389 thick profile analyzed in this study. This age would lead to a ^{10}Be concentration at 2 m depth
390 much higher than the inherited ^{10}Be concentration of 15,000 at/g quartz obtained from our
391 data. In this bedrock, the measured inherited ^{10}Be concentration corresponds to the
392 concentration obtained from a muonic exposure at approximately 4 m depth over ≈ 150 kyr.
393 A way to reconcile all the data, assuming the above determined average denudation rate of
394 22 mm/kyr , is that a thickness of 2 m was eroded 20 kyr ago and that a total resetting of the
395 bedrock ^{10}Be inventory must have occurred 150 kyr ago, which is consistent with the fact
396 that the penultimate Riss glaciation was probably more intense than the last Würm
397 glaciation in the mountains of central Europe (Dehnert et al., 2010).

398 The independent determination of regolith production and denudation rates from U-Th-Ra
399 isotopes and in situ ^{10}Be constitutes an interesting method for discussing the stability state

400 of a weathering profile on a millennial timescale. For the Strengbach case, the proposed
401 approach gives similar values for denudation rate (37 ± 15 T/km²/yr) and production rate
402 (30 ± 10 T/km²/yr), suggesting that at a millennial time scale, the regolith mass balance at the
403 summit of the catchment is close to steady state, even if it was perturbed 20 kyr ago. Such a
404 conclusion may indicate that the return to mass balance steady state is relatively fast in this
405 system, i.e., obtained in less than 20 kyr and/or that the erosive event that occurred 20 kyr
406 ago has only very transiently disturbed the processes controlling regolith formation at the
407 summit of the Strengbach watershed. The results may also suggest that the recent
408 anthropogenic perturbations linked to the 20th century, e.g., acid rain or the recent
409 afforestation efforts, which may have recently modified the cationic concentrations and
410 acidity of soil and stream waters in the watershed (Viville et al., 2012; Prunier et al., 2015),
411 have not perturbed the ¹⁰Be and U-Th-Ra long-term records.

412 Very few other studies combining U-series disequilibrium and cosmonuclides methodology
413 exist for other sites, even when including those involving the meteoritic ¹⁰Be approach
414 (Table 4). In addition, these other studies usually dealt with more superficial regolith and
415 different sample sets for isotopic analyses. However, despite these limitations, the data
416 indicate that in all the investigated mid-mountain catchments, which are characterized by
417 different climatic and tectonic settings, there is a fairly good consistency between the long-
418 term regolith production and denudation rates (Table 4). This seems to be especially true at
419 the ridge-tops and/or hill-crests of watersheds, where geochronological interpretations are
420 likely less affected by colluvial transport and deposition. Altogether, even if such a
421 conclusion remains preliminary, the current data suggest that the long-term regolith
422 evolution could be commonly at steady state.

423 **6.3 Comparison of millennial and present-day weathering and erosion rates**

424 Because U-series and ^{10}Be approaches integrate long-term processes, a substantial step to
425 understand the recent regolith evolution could be provided by the comparison of long-term
426 weathering and erosion rates with present-day estimates. As established by Riebe et al.
427 (2003), the knowledge of denudation rates determined by cosmogenic nuclide, combined
428 with the geochemical mass balance approaches and the definition of the chemical depletion
429 fraction (CDF), allow to distinguish the chemical and physical components of the total
430 denudation. This approach is predicated on an assumption of steady state, which is
431 supported by the consistency between U-series and ^{10}Be results. The total weathering rate in
432 $\text{T}/\text{km}^2/\text{yr}$ is as follows:

$$W = D \left(1 - \frac{C(\text{Ti})_{\text{rock}}}{C(\text{Ti})_{\text{soil}}} \right) = D \times CDF \quad (11)$$

433

434 where D is the mean denudation rate in $\text{T}/\text{km}^2/\text{yr}$ inferred from the cosmogenic ^{10}Be and
435 $C(\text{Ti})_{\text{rock}}$ and $C(\text{Ti})_{\text{soil}}$ are the concentrations of titanium (considered an immobile
436 element) in the bedrock and in the soil, respectively. The application of this approach to the
437 bedrock and the soil levels of the studied weathering profile leads to a CDF value of 0.22
438 when using for the average Ti concentrations of the bedrock and soil levels. A maximum CDF
439 value of 0.30 is obtained by using the lowest Ti concentrations measured in the bedrock and
440 the highest concentrations in the soil. Similar calculations can be made with Zr, which can
441 also be considered an immobile element in the Strengbach catchment (Rihs et al., 2011):
442 CDF values between 0.13 and 0.25 are obtained according to whether the average
443 concentration values or the extreme values are used for each level. These different

444 calculations indicate that at the profile scale, long-term chemical weathering accounts for 13
445 to 30 % of the total denudation, which yields a long-term chemical weathering flux of
446 between 5 and 11 T/km²/yr and consequently a long-term erosion flux of between 26 and 32
447 T/km²/yr. Therefore, physical erosion is the main process controlling the loss of regolith.

448 The above weathering flux calculations can be easily adapted to calculate the long-term
449 weathering flux of a specific chemical element by using the mean denudation rate (D), the
450 elemental concentrations within the bedrock ($C(x)_{bedrock}$) and the tau values (τ_x) in the
451 upper soil (Riebe et al., 2003):

$$W_x = D * C(x)_{bedrock} * (-\tau_x) \quad (12)$$

452

453 Based on this approach, long-term weathering fluxes of approximately 3 ± 2 T/km²/yr for Si
454 and 0.7 ± 0.47 T/km²/yr for cations can be estimated from the geochemical variations along
455 the regolith profile at the watershed summit. Similarly, the regular analyses of the dissolved
456 fluxes and the sediment loads carried by the Strengbach stream allow for estimation of the
457 current erosion and weathering rates at the watershed scale. The combination of the
458 suspended and bed load monitoring yields a total erosion rate of 5 ± 1 T/km²/yr at the
459 watershed outlet (Viville et al., 2012). By correcting the net flux for basic cations from
460 atmospheric deposition, a cationic weathering flux of 1.98 ± 0.2 T/km²/yr and a Si
461 weathering flux of 2.89 ± 0.3 T/km²/yr are estimated (Viville et al., 2012). The current
462 exported flux for Si determined at the watershed outlet is surprisingly very close to the long-
463 term Si weathering flux associated with regolith formation inferred for the watershed
464 summit. This consistency means that the first-order chemical weathering, which is controlled
465 by the rates of primary mineral dissolution and secondary mineral precipitation, is rather

466 spatially uniform and stable in time. In contrast, the current cationic flux in the Strengbach
467 stream seems to be higher than the long-term flux determined at the profile scale for basic
468 cations. This difference may be due to a recent increase in basic cation leaching from
469 Strengbach soils, possibly triggered by the acidic atmospheric inputs and/or the forest
470 management evolution experienced by the Strengbach catchment in recent decades (Viville
471 et al., 2012; Prunier et al., 2015). In contrast to the weathering rates, the long-term erosion
472 rate determined from ^{10}Be and CDF data (approximately 30 T/km²/yr) is clearly higher than
473 the current erosion rate determined in the Strengbach stream (approximately 5 T/km²/yr;
474 Viville et al., 2012). The latter value is certainly an underestimate, as the suspended load was
475 sampled only once every one or two weeks, which probably does not allow for a correct
476 estimate of the suspended load exported during flood events. A more recent study of the
477 erosion fluxes exported from the Strengbach watershed at its outlet, including an accurate
478 determination of the suspended load exported from the watershed during flood events,
479 yielded an erosion rate no higher than 10 T/km²/yr (Cotel et al., 2016). Regarding the
480 sampling frequency developed in the latter study, and even if the bed load is always difficult
481 to estimate precisely, an additional bias for the current erosion rates by a factor of three
482 seems improbable. Thus, unlike weathering fluxes, the long-term erosion rate determined at
483 the watershed summit and the present-day rate at the watershed scale are most likely
484 different. Such a discrepancy is certainly not surprising, and can result from spatial
485 heterogeneity in the erosion rate at the watershed scale, with high erosion rates along the
486 main crests possibly counterbalanced by sediment storage downhill. It could also result from
487 temporal variability in the physical erosion rate, with, for instance, high erosion rates during
488 cold conditions, probably persisting long after the LGM, followed by lower erosion rates due

489 to stabilization of the regolith by soil and vegetation cover development during the
490 Holocene.

491 As illustrated in the Strengbach case, this combination of U-series, in situ ^{10}Be and stream
492 monitoring allows for discussing the weathering and erosion variability at different spatial
493 and temporal scales. Another site where a similar comparison is possible is the Rio Icacos
494 watershed (Table 5 in Chabaux et al., 2013). Similar to the Strengbach catchment, an analysis
495 suggests relatively similar long-term and short-term weathering rates, whereas significant
496 differences exist between long-term denudation rates inferred from ^{10}Be data and current
497 erosion rates determined from sediment monitoring, which is also similar to the Strengbach
498 catchment (Table 4). However, in this case, unlike the Strengbach catchment, the current
499 erosion rates are higher than the long-term ones. This large variability in the physical erosion
500 fluxes through time is also suggested in a few other studies. In the Susquehanna Shale Hills
501 Observatory, it has been proposed that current erosion rates may be lower than previous
502 conditions because deep sediments in the valley floor appear to retain a record of enhanced
503 colluvial transport in the past (West et al., 2013). In Australia, longer sediment residence
504 times have been proposed for the Murrumbidgee River during warm periods, in association
505 with the development of vegetation cover and a decrease in erosion (in Dosseto and
506 Schaller, 2016). Even if, once again, there are very few sites where long-term trends are
507 compared to short-term trends, it seems that mid-mountain watersheds that experienced
508 glacial or periglacial conditions during the LGM (Strengbach, SSHO or Australian upper
509 watersheds) recorded a decrease in erosion rates with the onset of Holocene. In contrast, in
510 the Rio Icacos watershed, characterized by warmer conditions and hence unaffected by
511 periglacial processes, the current erosion rates are faster (Table 4). Thus, the above data
512 support the assumption deduced from the Strengbach case that the erosion rates have been

513 more variable than the chemical weathering rates during the Quaternary. The data might
514 also suggest a possible role of periglacial processes in the erosional response to Quaternary
515 climatic variations.

516 **7 Conclusions**

517 The study performed on a weathering profile sampled at the summit of the Strengbach
518 catchment illustrates the interesting results of the combined analyses of in situ ^{10}Be
519 concentrations, ^{238}U - ^{234}U - ^{230}Th - ^{226}Ra disequilibria and major and trace element
520 concentrations. As summarized in Figure 5, this combination is a powerful methodology for
521 recovering key parameters of the long-term regolith evolution. This approach suggests that
522 the long-term regolith evolution in the Strengbach watershed is relatively close to steady
523 state, despite recent anthropogenic perturbations. In addition, in regard to the mineralogical
524 properties of the profile and implicit assumptions of the U-Th-Ra modeling, it appears that in
525 this site (as well as in many other forest contexts), the bedrock is the most suitable place to
526 quantify the regolith production rate using the U-Th-Ra methodology. The results also
527 highlight the importance of having a sufficiently dense sampling strategy along the regolith
528 depth profile to recover the Quaternary polyphase history of the regolith from the analysis
529 and modeling of in situ ^{10}Be . In combination with the above data, geochemical and mass
530 balance calculations performed in the Strengbach stream and along the weathering profile
531 allow for investigating the regolith evolution at different spatial and temporal scales. The
532 results indicate that physical erosion is the dominant process of regolith loss in the
533 Strengbach catchment and has probably varied much more than chemical weathering
534 through time. Although very few sites with U-series, in situ ^{10}Be and stream monitoring data
535 are available for comparison, the current data suggest that (1) mass balance steady state of

536 regolith can be commonly achieved in soil mantled landscapes and (2) physical erosion has
537 exhibited higher variability than chemical weathering over the last 10-150 kyr. The combined
538 U-series and in situ ^{10}Be analyses in high spatial resolution depth profiles could become a
539 powerful approach in the future for providing new quantitative insights on weathering
540 profile dynamics and regolith erosive history over Holocene and Late Pleistocene time
541 periods. The association of these approaches with the monitoring of water chemistry and
542 sediment fluxes at watershed outlets seems also important to correctly positioning the
543 present-day erosion and weathering rates relative to the past rates recorded by the U-Th-Ra
544 and in situ ^{10}Be inventories.

545 **Acknowledgments**

546 This work has been supported by the funding of a Ph.D. scholarship to J. Ackerer from the
547 Region Alsace, France and the BRGM, Orléans, France. ^{10}Be ratios were measured at the
548 ASTER AMS national facility (CEREGE, Aix-en-Provence), supported by INSU-CNRS, IRD and
549 CEA. This study was financially supported by funding from the REALISE program to F.
550 Chabaux. We are grateful to A. Aubert and N. Maubec for the X-ray diffraction
551 measurements and interpretations and to R. Boutin for the analysis of the major and trace
552 element concentrations. We also thank M. Granet and T. Perrone for their help during
553 sample preparation and P. Stille, M.C. Pierret and C. Bosia for discussions during the course
554 of the work. We sincerely thank S. Brown and two anonymous reviewers, as well as the
555 Editor D. Vance, for their very constructive and thoughtful comments. This is a LHyGeS-EOST
556 contribution.

557 **Table and figure captions**

558 Table 1: Some chemical and physical characteristics of the studied weathering profile. Major and
559 trace element concentrations were determined by conventional tetraborate alkaline fusion followed
560 by mass spectrometry and atomic emission spectrometry measurements (ICP-MS and ICP-AES
561 procedure) (uncertainty <5 % for major element and <10 % for trace element concentrations). STR13-
562 53² is a dissolution powder duplicate. STR13-53³ is a quartering duplicate that encompasses the
563 whole crushing process.

564 Table 2: U-series data. U and Th concentrations are calculated from isotopic dilution. The
565 uncertainties are at the 2σ level: 0.2 % and 0.5 % for U and Th concentrations, 0.2 % for ($^{234}\text{U} / ^{238}\text{U}$), 1
566 % for ($^{230}\text{Th} / ^{232}\text{Th}$), 1.5 % for ($^{230}\text{Th} / ^{234}\text{U}$) and 1.7 % for ($^{226}\text{Ra} / ^{230}\text{Th}$) activity ratios. STR13-53² is a
567 dissolution powder duplicate. STR13-53³ is a quartering duplicate that encompasses the whole
568 crushing process. For the activity ratio calculation, the following radioactivity constants were used:
569 $\lambda_{232}=4.948\times 10^{-11} \text{ yr}^{-1}$, $\lambda_{230}=9.158\times 10^{-6} \text{ yr}^{-1}$, $\lambda_{234}=2.826\times 10^{-6} \text{ yr}^{-1}$, $\lambda_{238}=1.551\times 10^{-10} \text{ yr}^{-1}$, and $\lambda_{226}=4.335\times 10^{-4}$
570 yr^{-1} (Akovali, 1996; Cheng et al., 2000).

571 Table 3: In situ ^{10}Be data for the studied weathering profile. The elevation is 1147 m a.s.l. The latitude
572 and longitude are $48^{\circ}12'29.4''\text{N}$ and $7^{\circ}11'30.3''\text{E}$, respectively. There is no shielding correction due to
573 the summit location of the profile. The surface production rates were determined with the CRONUS
574 online calculator (Balco et al., 2008) and are 12.17 at/g/yr and 0.266 at/g/yr for spallation and
575 muons, respectively. The total ^9Be represents the carrier and natural ^9Be of the samples (ICP-AES
576 measurements). AMS analysis calibration was performed with a BeO NIST 4325 standard at ASTER.
577 $^{10}\text{Be}/^9\text{Be}$ are blank corrected values. Uncertainties include AMS analysis, carrier mass and blank
578 uncertainties.

579
580 Table 4: Synthesis table of the studied sites that allow for U-series and ^{10}Be results comparison.
581 When rates are not provided in T/km²/yr, conversions from mm/kyr to T/km²/yr have been
582 performed by assuming a regolith bulk mean density of 1700 kg/m³. (1) This study. (2) Cotel et al.,
583 2016. (3) Ma et al., 2010. (4) West et al., 2013. (5) Jin et al., 2010. (6) Schoonejans et al., 2016. (7) Dosseto
584 et al., 2008. (8) Heimsath et al., 2000. (9) Chabaux et al., 2013. (10) Brown et al., 1995. (11) McDowell and
585 Asbury, 1994. ^{10}Be denudation rates have been determined by in situ ^{10}Be data, except for West et
586 al., 2013, where meteoritic ^{10}Be has been used.

587 Figure 1: a) Regional map of the Vosges massif and location of the Strengbach catchment. b) Contour
588 of the Strengbach watershed. c) Topographic map of the Strengbach watershed and location of the

589 studied weathering profile (map from OHGE). d) Sampling of the weathering profile. The pedological
590 observation led to division of the weathering profile into 3 zones: the soil from 0 to 50 cm, the
591 saprolite from 50 to 100 cm and the granitic weathered bedrock from 100 to 200 cm. Each box in the
592 column represents a collected sample. Red and blue dots indicate samples for which isotopic U-Th-Ra
593 and in situ ^{10}Be analyses have been performed, respectively. Green dots indicate samples for which
594 thin sections have been performed.

595 Figure 2: a) Mass transfer coefficients calculated from equation 7. The uncertainty is calculated from
596 elemental concentration uncertainty propagation and is <20 % (error bars show 20 % level). b) U/Th
597 ratio. The U and Th concentrations are calculated from isotopic dilution. The uncertainty is 0.2 % for
598 U, 0.5 % for Th and is within size point. c) Th/Ti ratio. The Ti and Th concentrations are calculated
599 from alkaline fusion. The uncertainty is <15 % (error bars show 15 % level).

600 Figure 3: a) Bulk density calculated by combining the fine fraction density and the density of blocks
601 with respect to the proportion of blocks in each horizon. For the bedrock and the blocks of granite, a
602 constant density of 2700 kg/m^3 is assumed. b) Volumetric strain index calculated from equation 9.
603 Uncertainty is calculated from elemental concentration uncertainty propagation and is <10 % (error
604 bars show 10 % level) c) ^{10}Be depth profile. In blue: measured ^{10}Be concentrations. Uncertainty is <5
605 % (error bars show 5 % level). In red: best fit obtained from optimization by Levenberg-Marquardt
606 algorithm. In grey: modeled ^{10}Be concentrations without taking into account soil expansion.

607 Figure 4: ($^{234}\text{U}/^{238}\text{U}$), ($^{230}\text{Th}/^{234}\text{U}$) and ($^{226}\text{Ra}/^{230}\text{Th}$) radioactive activity ratios along the weathering
608 profile. In blue: experimental data. The uncertainties are at the 2σ level: 0.2 % for ($^{234}\text{U}/^{238}\text{U}$), 1.5 %
609 for ($^{230}\text{Th}/^{234}\text{U}$) and 1.7 % for ($^{226}\text{Ra}/^{230}\text{Th}$) measured activity ratios. In red: best fit obtained from
610 numerical optimization. Calculated coefficients: $k_{238} = 4.81 * 10^{-6} \pm 3.68 * 10^{-7}$, $k_{234} = 5.47 * 10^{-6} \pm 9.20 * 10^{-7}$,
611 $k_{226} = 2.22 * 10^{-5} \pm 4.44 * 10^{-6}$, $f_{238} = 1.63 * 10^{-6} \pm 4.00 * 10^{-7}$, $f_{234} = 2.76 * 10^{-6} \pm 8.96 * 10^{-7}$
612 and $f_{226} = 6.61 * 10^{-6} \pm 2.20 * 10^{-6}$ (2σ level, expressed in yr^{-1}).
613 Calculated weathering age is approximately 69,000 yr for the modeled section.

614 Figure 5: Summary of the methodologies applied to the regolith profile at the Strengbach catchment
615 summit. Combined approaches allow for constraining the long-term evolution of the profile with
616 comparison of both regolith production and denudation rates.

617

618 **References**

- 619 Akovali, Y. A. (1996). Nuclear data sheets for A= 226. *Nuclear Data Sheets*, 77(2), 433-470.
- 620 Anderson, R. S., Repka, J. L., & Dick, G. S. (1996). Explicit treatment of inheritance in dating
621 depositional surfaces using in situ ¹⁰Be and ²⁶Al. *Geology*, 24(1), 47-51.
- 622 Balco, G., Stone, J. O., Lifton, N. A., & Dunai, T. J. (2008). A complete and easily accessible
623 means of calculating surface exposure ages or erosion rates from ¹⁰Be and ²⁶Al
624 measurements. *Quaternary geochronology*, 3(3), 174-195.
- 625 Banwart, S., Bernasconi, S. M., Bloem, J., Blum, W., Brandao, M., Brantley, S., ... & Zhang, B.
626 (2011). Soil processes and functions in critical zone observatories: hypotheses and
627 experimental design. *Vadose Zone Journal*, 10(3), 974-987.
- 628 Brantley, S. L., Goldhaber, M. B., & Ragnarsdottir, K. V. (2007). Crossing disciplines and scales
629 to understand the critical zone. *Elements*, 3(5), 307-314.
- 630 Braucher, R., Del Castillo, P., Siame, L., Hidy, A. J., & Bourlès, D. L. (2009). Determination of
631 both exposure time and denudation rate from an in situ-produced ¹⁰Be depth
632 profile: a mathematical proof of uniqueness. Model sensitivity and applications to
633 natural cases. *Quaternary Geochronology*, 4(1), 56-67.
- 634 Brimhall, G. H., Ford, C., Bratt, J., Taylor, G., & Warin, O. (1991). Quantitative geochemical
635 approach to pedogenesis: importance of parent material reduction, volumetric
636 expansion, and eolian influx in lateritization. *Geoderma*, 51(1), 51-91.
- 637 Brocard, G. Y., Van Der Beek, P. A., Bourlès, D. L., Siame, L. L., & Mugnier, J. L. (2003). Long-
638 term fluvial incision rates and postglacial river relaxation time in the French Western
639 Alps from ¹⁰Be dating of alluvial terraces with assessment of inheritance, soil
640 development and wind ablation effects. *Earth and Planetary Science Letters*, 209(1),
641 197-214.

642 Brown, E. T., Stallard, R. F., Larsen, M. C., Raisbeck, G. M., & Yiou, F. (1995). Denudation rates
643 determined from the accumulation of in situ-produced ^{10}Be in the Luquillo
644 Experimental Forest, Puerto Rico. *Earth and Planetary Science Letters*, *129*(1), 193-
645 202.

646 Chabaux F., Riotte J., Dequincey O. (2003). U-Th-Ra fractionation during weathering and river
647 transport, *Rev Mineral. Geochem.*, *52*, 533-576.

648 Chabaux, F., Ma, L., Stille, P., Pelt, E., Granet, M., Lemarchand, D., ... & Brantley, S. L. (2011).
649 Determination of chemical weathering rates from U series nuclides in soils and
650 weathering profiles: Principles, applications and limitations. *Applied Geochemistry*,
651 *26*, S20-S23.

652 Chabaux, F., Blaes, E., Stille, P., di Chiara Roupert, R., Pelt, E., Dosseto, A., ... & Brantley, S. L.
653 (2013). Regolith formation rate from U-series nuclides: Implications from the study of
654 a spheroidal weathering profile in the Rio Icacos watershed (Puerto Rico). *Geochimica
655 et Cosmochimica Acta*, *100*, 73-95.

656 Cheng, H., Edwards, R. L., Hoff, J., Gallup, C. D., Richards, D. A., & Asmerom, Y. (2000). The
657 half-lives of uranium-234 and thorium-230. *Chemical Geology*, *169*(1), 17-33.

658 Cotel S., Viville D., Pierret M.C., Benarioumlil S., Chabaux F. (2016) Evaluation of fluxes of
659 suspended matters and bedload in the small granitic Strengbach catchment (Vosges
660 massif, France). Geophysical Research Abstracts Vol. 18, EGU2016-13179.

661 Cui L., Liu C.Q., Xu S., Zhao Z.-Q., Liu T.-Z., Liu W.-J., Zhang Z.-J. (2016) Subtropical
662 denudation rates of granitic regolith along a hill ridge in Longnan, SE China derived
663 from cosmogenic nuclides depth-profiles, *Journal of Asian Earth Sciences* *117*, 146-
664 152

665 Dehnert, A., Preusser, F., Kramers, J. D., Akcar, N., Kubik, P. W., Reber, R., & Schluechter, C.
666 (2010). A multi-dating approach applied to proglacial sediments attributed to the
667 Most Extensive Glaciation of the Swiss Alps. *Boreas*, 39(3), 620-632.

668 Dequincey, O., Chabaux, F., Clauer, N., Sigmarsson, O., Liewig, N., & Leprun, J. C. (2002).
669 Chemical mobilizations in laterites: evidence from trace elements and ²³⁸U-²³⁴U-
670 ²³⁰Th disequilibria. *Geochimica et Cosmochimica Acta*, 66(7), 1197-1210.

671 Dosseto, A., Turner, S. P., & Chappell, J. (2008). The evolution of weathering profiles through
672 time: new insights from uranium-series isotopes. *Earth and Planetary Science Letters*,
673 274(3), 359-371.

674 Dosseto A., Buss H. and Suresh P. O. (2012) Rapid regolith formation over volcanic bedrock
675 and implications for land-scape evolution. *Earth Planet. Sci. Lett.* 337, 47–55.

676 Dosseto, A., & Schaller, M. (2016). The erosion response to Quaternary climate change
677 quantified using uranium isotopes and in situ-produced cosmogenic nuclides. *Earth-*
678 *Science Reviews*, 155, 60-81.

679 Egli, M., Mirabella, A., Sartori, G., Zanelli, R., & Bischof, S. (2006). Effect of north and south
680 exposure on weathering rates and clay mineral formation in Alpine soils. *Catena*,
681 67(3), 155-174.

682 Etienne, D., Ruffaldi, P., Dupouey, J. L., Georges-Leroy, M., Ritz, F., & Dambrine, E. (2013).
683 Searching for ancient forests: A 2000 year history of land use in northeastern French
684 forests deduced from the pollen compositions of closed depressions. *The Holocene*,
685 23(5), 678-691.

686 Fichter, J., Turpault, M. P., Dambrine, E., & Ranger, J. (1998). Mineral evolution of acid forest
687 soils in the Strengbach catchment (Vosges mountains, NE France). *Geoderma*, 82(4),
688 315-340.

689 Ferrier, K. L., & Kirchner, J. W. (2008). Effects of physical erosion on chemical denudation
690 rates: a numerical modeling study of soil-mantled hillslopes. *Earth and Planetary*
691 *Science Letters*, 272(3), 591-599.

692 Gangloff S., Stille P., Pierret M-C., Weber T., Chabaux F. (2014) Characterization and
693 evolution of dissolved organic matter in acidic forest soil and its impact on the
694 mobility of major and trace elements (case of the Strengbach watershed) *Geochimica*
695 *et Cosmochimica Acta*, 130, 21-41.

696 Gontier, A., Rihs, S., Chabaux, F., Lemarchand, D., Pelt, E., Turpault, M.-P. (2015) Lack of
697 bedrock grain size influence on the soil production rate, *Geochimica et Cosmochimica*
698 *Acta*, 166, 146-164.

699 Granet, M., Chabaux, F., Stille, P., Dosseto, A., France-Lanord, C., & Blaes, E. (2010). U-series
700 disequilibria in suspended river sediments and implication for sediment transfer time
701 in alluvial plains: the case of the Himalayan rivers. *Geochimica et Cosmochimica Acta*,
702 74(10), 2851-2865.

703 Gy, P. M. (1992). *Sampling of heterogeneous and dynamic material systems: theories of*
704 *heterogeneity, sampling and homogenizing*. Elsevier.

705 Heimsath, A. M., Chappell, J., Dietrich, W. E., Nishiizumi, K., & Finkel, R. C. (2000). Soil
706 production on a retreating escarpment in southeastern Australia. *Geology*, 28(9),
707 787-790.

708 Heyman, B. M., Heyman, J., Fickert, T., & Harbor, J. M. (2013). Paleo-climate of the central
709 European uplands during the last glacial maximum based on glacier mass-balance
710 modeling. *Quaternary Research*, 79(1), 49-54.

711 Jin, L., Ravella, R., Ketchum, B., Bierman, P. R., Heaney, P., White, T., & Brantley, S. L. (2010).
712 Mineral weathering and elemental transport during hillslope evolution at the

713 Susquehanna/Shale Hills Critical Zone Observatory. *Geochimica et Cosmochimica*
714 *Acta*, 74(13), 3669-3691.

715 Kim, K. J., & Englert, P. A. J. (2004). Profiles of in situ ¹⁰Be and ²⁶Al at great depths at the
716 Macraes Flat, East Otago, New Zealand. *Earth and Planetary Science Letters*, 223(1),
717 113-126.

718 Leroy, S. A. G., ZOLITSCHKA, B., NEGENDANK, J. F., & Seret, G. U. Y. (2000). Palynological
719 analyses in the laminated sediment of Lake Holzmaar (Eifel, Germany): duration of
720 Lateglacial and Preboreal biozones. *Boreas*, 29(1), 52-71.

721 Ma, L., Chabaux, F., Pelt, E., Blaes, E., Jin, L., & Brantley, S. (2010). Regolith production rates
722 calculated with uranium-series isotopes at Susquehanna/Shale Hills Critical Zone
723 Observatory. *Earth and Planetary Science Letters*, 297(1), 211-225.

724 Marquardt, D. W. (1963). An algorithm for least-squares estimation of nonlinear parameters.
725 *Journal of the Society for Industrial & Applied Mathematics*, 11(2), 431-441.

726 McDowell, W. H., & Asbury, C. E. (1994). Export of carbon, nitrogen, and major ions from
727 three tropical montane watersheds. *Limnology and oceanography*, 39(1), 111-125.

728 Mercier, J. L., Bourlès, D. L., Kalvoda, J., Braucher, R., & Paschen, A. (1999). Deglaciation of
729 the Vosges dated using ¹⁰Be. *Acta Universitatis Carolinae–Geographica*, 2, 139-155.

730 Nishiizumi, K., Winterer, E. L., Kohl, C. P., Klein, J., Middleton, R., Lal, D., & Arnold, J. R.
731 (1989). Cosmic ray production rates of ¹⁰Be and ²⁶Al in quartz from glacially polished
732 rocks. *Journal of Geophysical Research: Solid Earth (1978–2012)*, 94(B12), 17907-
733 17915.

734 Pelt, E., Chabaux, F., Stille, P., Innocent, C., Ghaleb, B., Gérard, M., & Guntzer, F. (2013).
735 Atmospheric dust contribution to the budget of U-series nuclides in soils from the
736 Mount Cameroon volcano. *Chemical Geology*, 341, 147-157.

737 Prunier J., Chabaux F., Stille P., Pierret MC, Viville D., Gangloff S. (2015) Monitoring of
738 geochemical and isotopic (Sr,U) signatures in soil solutions for the evaluation of soil
739 weathering evolution (the Strengbach case) *Chemical Geology*, 417, 289–305.

740 Riebe, C. S., Kirchner, J. W., & Finkel, R. C. (2003). Long-term rates of chemical weathering
741 and physical erosion from cosmogenic nuclides and geochemical mass balance.
742 *Geochimica et Cosmochimica Acta*, 67(22), 4411-4427.

743 Rihs, S., Prunier, J., Thien, B., Lemarchand, D., Pierret, M. C., & Chabaux, F. (2011). Using
744 short-lived nuclides of the U-and Th-series to probe the kinetics of colloid migration
745 in forested soils. *Geochimica et Cosmochimica Acta*, 75(23), 7707-7724.

746 Schaller, M., Von Blanckenburg, F., Veldkamp, A., Tebbens, L. A., Hovius, N., & Kubik, P. W.
747 (2002). A 30 000 yr record of erosion rates from cosmogenic ¹⁰Be in Middle
748 European river terraces. *Earth and Planetary Science Letters*, 204(1), 307-320.

749 Schoonejans, J., Vanacker, V., Opfergelt, S., Granet, M., & Chabaux, F. (2016). Coupling
750 uranium series and ¹⁰Be cosmogenic radionuclides to evaluate steady-state soil
751 thickness in the Betic Cordillera. *Chemical Geology*.

752 Seret, G., Dricot, E., & Wansard, G. (1990). Evidence for an early glacial maximum in the
753 French Vosges during the last glacial cycle. *Nature*, 346(6283), 453-456.

754 Siame, L., Bellier, O., Braucher, R., Sébrier, M., Cushing, M., Bourlès, D., & Yiou, F. (2004).
755 Local erosion rates versus active tectonics: cosmic ray exposure modelling in
756 Provence (south-east France). *Earth and Planetary Science Letters*, 220(3), 345-364.

757 Small, E.E., Anderson, R.S., Hancock, G.S., 1999. Estimates of the rate of regolith production
758 using ¹⁰Be and ²⁶Al from an alpine hillslope. *Geomorphology* 27, 131–150.

759 Stille P., Pourcelot L., Granet M., Pierret M.-C., Perrone Th, Morvan G., Chabaux F. (2011)
760 Deposition and migration of atmospheric Pb in soils from a forested silicate

761 catchment today and in the past (Strengbach case ; Vosges mountains) ; evidence
762 from ^{210}Pb activities and Pb isotope ratios. *Chem. Geol.* 289,140-153 (2011), doi:
763 10.1016/j.chemgeo.2011.07.021

764 Viville, D., Chabaux, F., Stille, P., Pierret, M. C., & Gangloff, S. (2012). Erosion and weathering
765 fluxes in granitic basins: the example of the Strengbach catchment (Vosges massif,
766 eastern France). *Catena*, 92, 122-129.

767 West, N., Kirby, E., Bierman, P., Slingerland, R., Ma, L., Rood, D., & Brantley, S. (2013).
768 Regolith production and transport at the Susquehanna Shale Hills Critical Zone
769 Observatory, part 2: insights from meteoric ^{10}Be . *Journal of Geophysical Research:*
770 *Earth Surface*, 118(3), 1877-1896.

771 WRB, 2006. International Union Soil Sciences Working Group WRB. 2006. World reference
772 base for soil resources 2006. World Soil Resources Reports No. 103. FAO, Rome
773

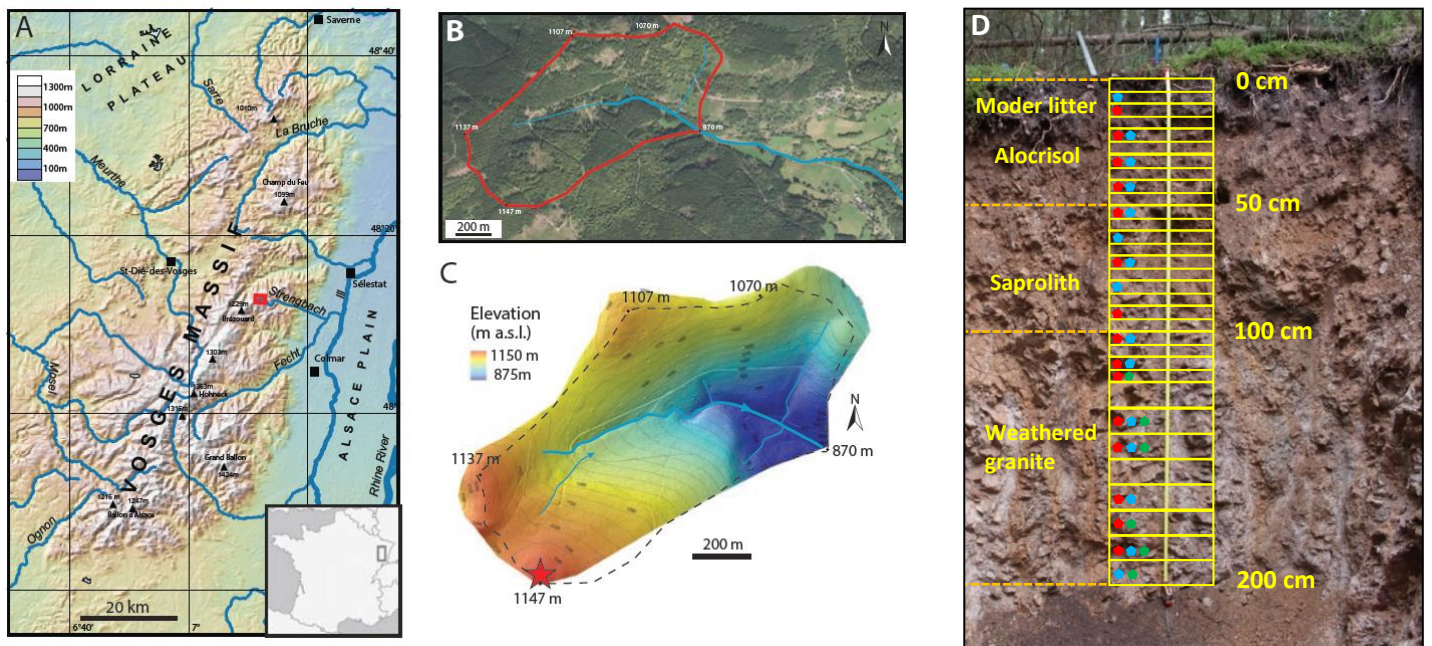


Figure 1

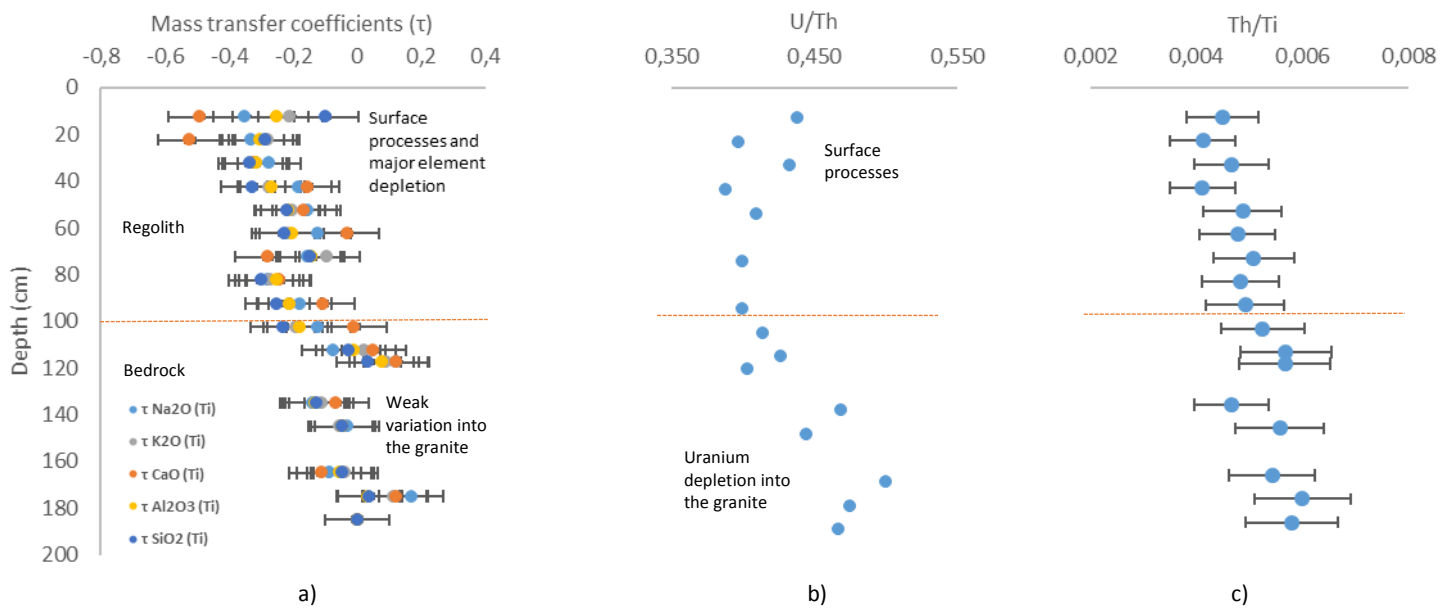


Figure 2

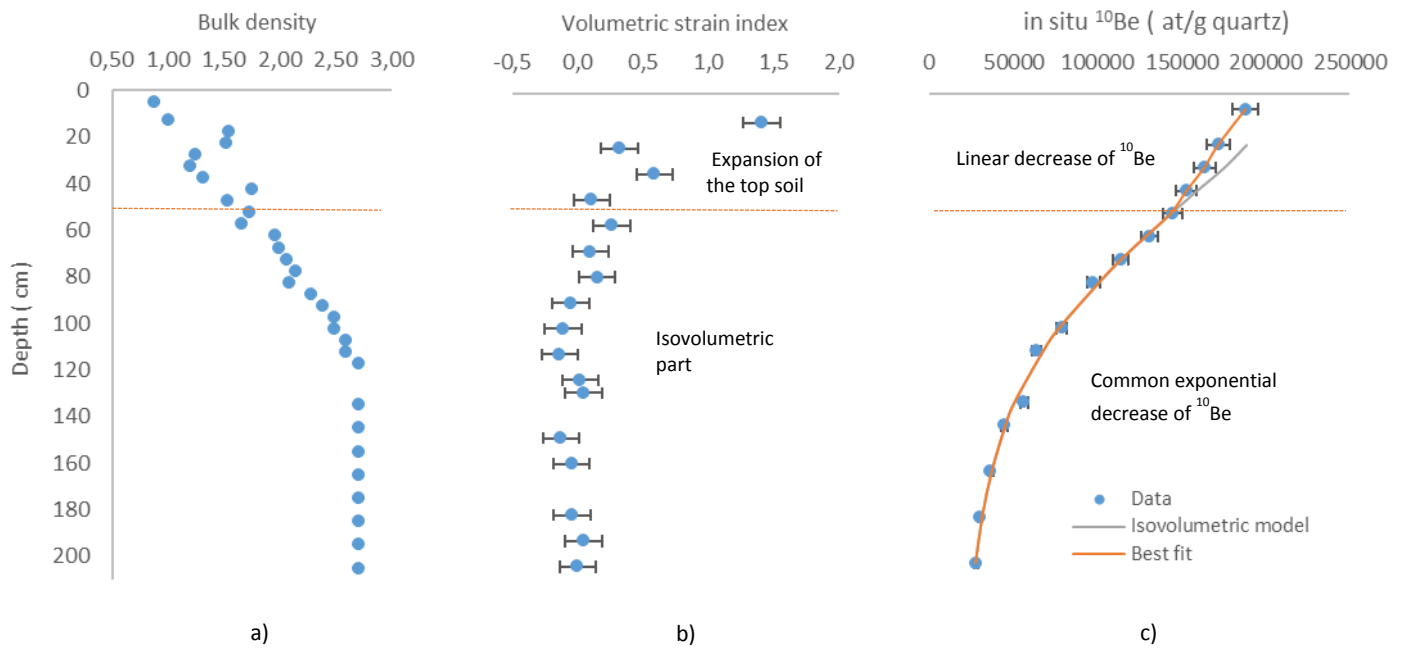


Figure 3

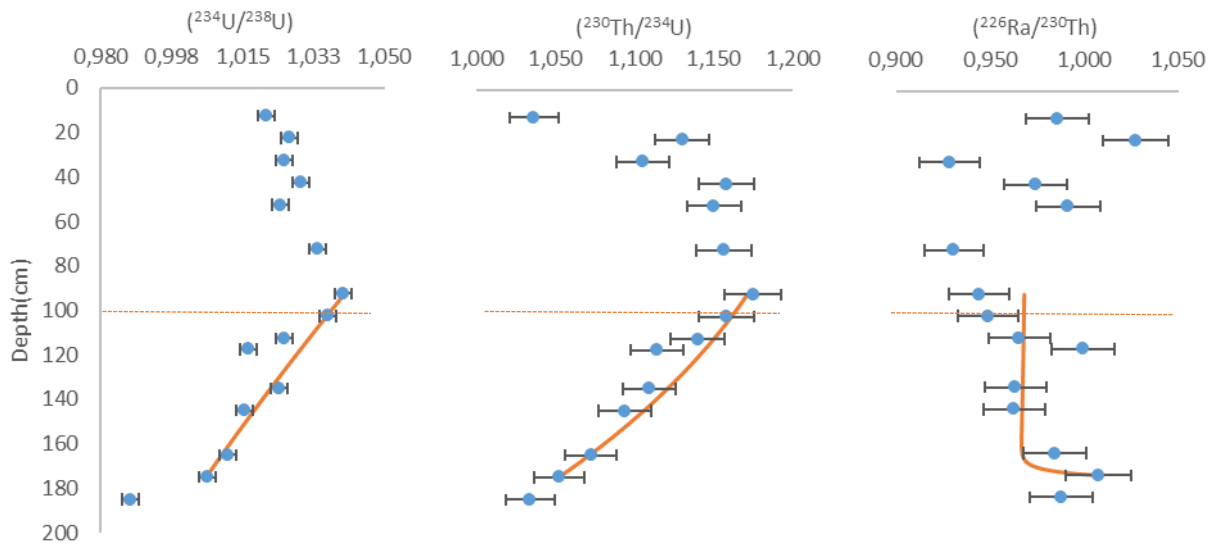


Figure 4

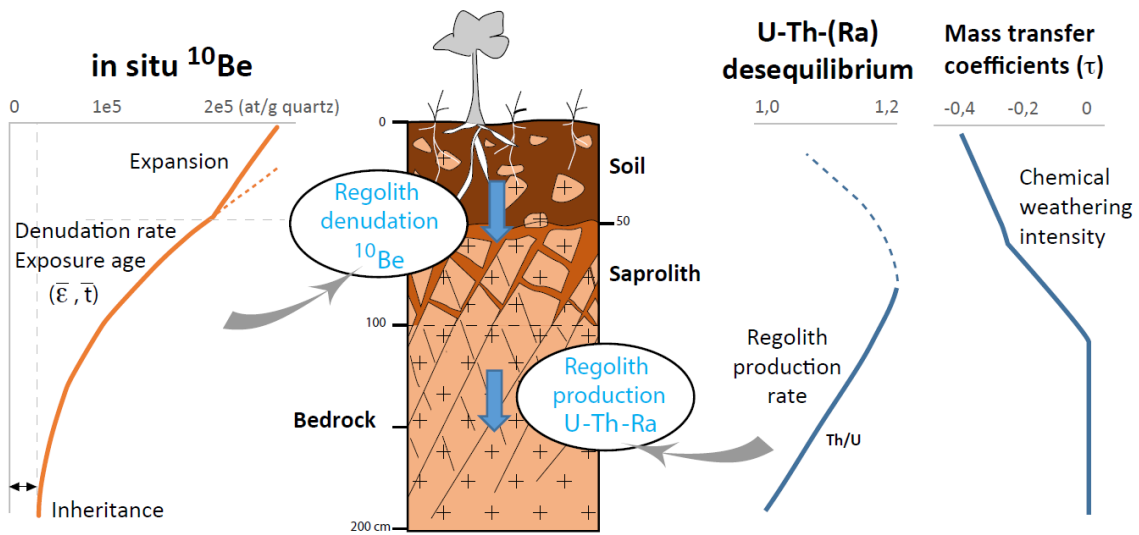


Figure 5

Sample	Depth (cm)	Quartz (%)	Plagioclase Feldspars (%)	K-feldspars (%)	Micas and illites (%)	Kaolinite (%)	Interstratified clays (%)	Hematite (%)
STR13-41	12.5	43	17	25	8	2	5	0
STR13-43	22.5	43	18	25	8	1	5	0
STR13-45	32.5	40	20	23	9	2	6	0
STR13-47	42.5	37	22	26	8	2	5	0
STR13-49	52.5	38	18	31	9	3	1	0
STR13-51	62.5	46	15	21	16	2	0	0
STR13-53	72.5	48	15	18	17	2	0	0
STR13-55	82.5	52	16	17	11	4	0	0
STR13-57	92.5	45	16	22	15	2	0	0
STR13-59	102.5	35	22	22	20	1	0	0
STR13-61	112.5	34	20	26	19	0	0	1
STR13-41B	117.5	37	18	29	14	2	0	0
STR13-42B	135	40	22	22	13	2	0	1
STR13-43B	145	33	19	30	14	2	0	2
STR13-45B	165	37	22	28	11	2	0	0
STR13-47B	185	32	20	29	17	2	0	0

Table 1

Sample	Depth (cm)	Type	Bulk density (g/cm ³)	SiO ₂ (%)	Al ₂ O ₃ (%)	CaO (%)	Na ₂ O (%)	K ₂ O (%)	MgO (%)	Fe ₂ O ₃ (%)	MnO (%)	TiO ₂ (%)	P ₂ O ₅ (%)	LOI (1000 °C) (%)	Ta (ppm)	Zr (ppm)
STR13-41	12.5	Soil	1.0	73.20	12.05	0.16	1.70	4.55	0.21	1.30	0.011	0.18	0.27	4.79	2.3	81.0
STR13-43	22.5	Soil	1.5	69.30	13.49	0.18	2.10	4.96	0.26	1.71	0.021	0.21	0.48	5.51	2.7	73.0
STR13-45	32.5	Soil	1.2	68.50	14.03	0.27	2.40	4.99	0.32	1.69	0.027	0.22	0.59	4.85	2.9	70.0
STR13-47	42.5	Soil	1.7	68.10	14.72	0.33	2.66	5.19	0.36	1.70	0.034	0.22	0.56	4.08	2.4	71.0
STR13-49	52.5	Soil	1.7	70.20	13.99	0.29	2.45	5.09	0.30	1.53	0.032	0.20	0.50	3.22	2.7	67.0
STR13-51	62.5	Saprolite	2.0	70.10	14.36	0.34	2.57	5.05	0.34	1.57	0.032	0.20	0.51	2.96	2.7	62.0
STR13-53	72.5	Saprolite	2.1	70.60	14.08	0.23	2.25	5.30	0.26	1.59	0.030	0.18	0.41	2.52	2.7	62.0
STR13-53 ²	72.5	Saprolite	2.1	71.20	13.94	0.32	2.39	5.07	0.34	1.60	0.030	0.19	0.42	-	-	-
STR13-53 ³	72.5	Saprolite	2.1	70.70	13.77	0.34	2.47	5.09	0.34	1.58	0.030	0.18	0.42	-	-	-
STR13-55	82.5	Saprolite	2.1	69.50	14.76	0.29	2.30	5.13	0.39	2.04	0.037	0.22	0.42	2.82	3.3	67.0
STR13-57	92.5	Saprolite	2.4	69.60	14.56	0.32	2.45	5.18	0.39	2.08	0.028	0.20	0.35	2.39	3.1	61.0
STR13-59	102.5	Bedrock	2.5	70.20	14.87	0.35	2.58	5.23	0.20	1.82	0.023	0.20	0.35	2.26	3.1	64.0
STR13-61	112.5	Bedrock	2.6	71.80	14.50	0.30	2.20	5.34	0.20	1.38	0.020	0.16	0.39	2.17	2.8	67.0
STR13-41B	117.5	Bedrock	2.7	71.60	14.80	0.30	2.50	5.35	0.20	1.19	0.020	0.15	0.34	1.97	2.5	64.0
STR13-42B	135	Bedrock	2.7	72.60	14.30	0.30	2.30	5.23	0.25	1.31	0.022	0.18	0.31	1.87	2.6	67.0
STR13-43B	145	Bedrock	2.7	72.60	14.38	0.28	2.37	5.10	0.26	1.25	0.027	0.17	0.33	1.59	2.8	70.0
STR13-45B	165	Bedrock	2.7	72.10	14.19	0.26	2.22	5.16	0.20	1.41	0.032	0.16	0.31	1.83	2.6	77.0
STR13-46B	175	Bedrock	2.7	71.80	14.20	0.30	2.60	5.46	0.26	1.27	0.017	0.15	0.33	1.7	2.5	70.0
STR13-47B	185	Bedrock	2.7	72.40	14.38	0.28	2.33	5.13	0.39	1.16	0.016	0.16	0.32	1.57	2.7	69.0

Table 2

Sample	Depth (cm)	U (ppm)	Th (ppm)	(²³⁴ U/ ²³⁸ U)	(²³⁰ Th/ ²³² Th)	(²³⁰ Th/ ²³⁴ U)	(²²⁶ Ra/ ²³⁰ Th)
STR13-41	12.5	3.417	7.800	1.021	1.412	1.036	0.986
STR13-43	22.5	3.621	8.904	1.026	1.433	1.130	1.027
STR13-45	32.5	4.224	9.752	1.025	1.495	1.105	0.928
STR13-47	42.5	3.830	9.636	1.029	1.440	1.158	0.974
STR13-49	52.5	3.763	9.179	1.024	1.471	1.150	0.992
STR13-53	72.5	3.528	8.622	1.034	1.486	1.156	0.931
STR13-53 ²	72.5	3.575	8.643	1.032	1.499	1.155	0.936
STR13-53 ³	72.5	3.462	8.699	1.034	1.454	1.162	0.936
STR13-57	92.5	3.841	9.387	1.040	1.519	1.175	0.944
STR13-59	102.5	4.155	9.810	1.036	1.544	1.158	0.949
STR13-61	112.5	3.884	9.111	1.025	1.517	1.140	0.966
STR13-41B	117.5	3.531	8.753	1.016	1.392	1.114	0.999
STR13-42B	135	3.957	8.433	1.024	1.623	1.109	0.963
STR13-43B	145	4.294	9.659	1.015	1.504	1.094	0.963
STR13-45B	165	4.601	9.193	1.011	1.653	1.072	0.984
STR13-46B	175	4.470	9.415	1.006	1.531	1.052	1.008
STR13-47B	185	4.269	9.149	0.987	1.451	1.034	0.988

Table 3

Sample	Depth (cm)	Integrated density (g/cm ³)	Mass of quartz (g)	Total ⁹ Be (mg)	¹⁰ Be/ ⁹ Be	± (%)	In situ ¹⁰ Be (at/g quartz)	± (%)
STR11-3	7	0.88	25.02	0.477	1.47E-13	3.1	188144	3.5
STR13-43	22.5	1.19	17.23	0.285	1.55E-13	3.4	171954	3.9
STR13-45	32.5	1.20	19.72	0.293	1.65E-13	4.0	163601	4.5
STR13-47	42.5	1.27	14.68	0.290	1.16E-13	3.9	153162	4.4
STR13-49	52.5	1.34	22.54	0.287	1.70E-13	3.9	144995	4.4
STR13-51	62.5	1.41	18.60	0.277	1.32E-13	3.3	131079	3.9
STR13-53	72.5	1.49	23.79	0.281	1.45E-13	3.8	114030	4.3
STR13-55	82.5	1.56	22.03	0.252	1.23E-13	3.2	97672	3.7
STR13-59	102.5	1.73	22.45	0.303	8.75E-14	3.9	78918	4.4
STR13-61	112.5	1.80	18.32	0.274	6.39E-14	4.0	63992	4.5
STR13-42B	135	1.96	29.31	0.291	8.49E-14	3.9	56360	4.4
STR13-43B	145	2.01	40.35	0.248	1.09E-13	5.2	44712	5.5
STR13-45B	165	2.09	38.00	0.278	7.48E-14	4.5	36532	4.9
STR13-47B	185	2.16	48.84	0.268	8.31E-14	3.9	30440	4.4
STR13-49B	205	2.21	57.09	0.280	8.55E-14	3.8	28057	4.3

Table 4

Site	Regolith production from U-series data (T/km ² /yr)	Regolith denudation from profile ¹⁰ Be data (T/km ² /yr)	Regolith denudation from river sediment ¹⁰ Be data (T/km ² /yr)	Erosion from river sediment load (T/km ² /yr)
Strengbach Catchment (France)	30 ± 10 ⁽¹⁾	37 ± 15 ⁽¹⁾	-	10 ± 2 ⁽²⁾
Susquehanna Shale Hills Observatory (United States)	29 ± 24 - 77 ± 20 ⁽³⁾	27 ± 10 - 34 ± 10 ⁽⁴⁾	39 ⁽⁵⁾	-
Betic Range (Spain)	12 ± 2 - 41 ± 9 ⁽⁶⁾	24 ± 5 - 39 ± 3 ⁽⁶⁾	-	-
Nunnock Catchment (Australia)	20 ± 3 - 130 ± 24 ⁽⁷⁾	12 ± 2 - 90 ± 5 ⁽⁸⁾	87 ± 9 ⁽⁸⁾	-
Rio Icacos Watershed (Porto Rico)	76 ± 20 ⁽⁹⁾	42 ± 15 - 85 ± 30 ⁽¹⁰⁾	73 ± 25 ⁽¹⁰⁾	300 ⁽¹¹⁾

Table 5

Mineralogical composition of the analyzed samples : methods and results

The mineralogical compositions of all the powdered 250- μm bulk samples were determined by XRD with a Siemens D5000 diffractometer with scanning from 4 to 84°, a space step of 0.04° and a time step of 18 s. The <2- μm clay fractions were separated by centrifugation and analyzed after air drying and treatment with glycol ethylene and hydrazine to distinguish illites, smectites, kaolinites and inter-stratified clays. The quantitative estimation of the proportion of the different minerals has been performed by the Rietveld method with the Siroquant software. The analytical uncertainty is approximately 3 % for the mass fraction of quartz and plagioclase and 5 % for the mass fraction of micas and clays.

The whole rock XRD analyses (Table Table EA1) show that quartz is the most abundant primary mineral (32 to 48 %), followed by K-feldspar (17 to 31 %), plagioclase feldspar (15 to 22 %), biotite and muscovite (approximately 9 %). Clay minerals include illites, smectites, interstratified illites/smectites and kaolinites, with a bulk clay fraction from a few % in the bedrock to 10 % in the upper soil (Table 1). Thin section observations confirm the presence of the above primary minerals (quartz, K-feldspar, plagioclase feldspar, biotite, and muscovite) and also indicate the presence of apatite, zircon, small amounts of aluminum silicates, hematite and rutile.

Table Caption

Table EA1 1: Bulk X-ray diffraction analysis for the studied weathering profile.